

Massive Data-Centric Parallelism in the Chiplet Era

Marcelo Orenes-Vera, Esin Tureci, David Wentzlaff and Margaret Martonosi

Princeton University, New Jersey, USA

{movera, esin.tureci, wentzlaf, mrm}@princeton.edu

Abstract—Traditionally, massively parallel applications have been executed on distributed systems, where computing nodes are distant enough that the parallelization schemes must minimize data communication and synchronization to achieve scalability. Mapping communication-intensive workloads to distributed systems require complicated problem partitioning and dataset pre-processing. With the current AI-driven trend of having thousands of interconnected processors per chip, there is an opportunity to re-think these communication-bottlenecked workloads. This bottleneck often arises from the data structure traversals, which cause irregular memory access patterns and poor cache locality.

Recent works have introduced task-based parallelization schemes to accelerate graph traversal and other sparse workloads. Data structure traversals are split into tasks, which are then pipelined across processing units (PUs). Dalorex demonstrated the highest scalability (up to thousands of PUs on a single chip) by having the entire dataset on-chip, scattered across PUs, and executing the tasks at the PU where the data is local. However, it also raised many questions on how to scale to larger datasets when all the memory is on-chip, and at what cost.

To address these challenges, we propose a scalable architecture composed of a grid of Data-Centric Reconfigurable Array (DCRA) chiplets. Package-time reconfiguration enables creating chip products that optimize for different target metrics, such as time-to-solution, energy, or cost, while software reconfigurations avoid network saturation when scaling to millions of PUs across many chip packages. We evaluate six applications and four datasets, with several configurations and memory technologies to provide a detailed analysis of the performance, power and cost of data-local execution at scale. Our parallelization of Breadth-First-Search with RMat-26 across a million PUs—the largest of the literature—reaches 3323 GTEPS.

I. INTRODUCTION

In the last decade, we have seen AI workloads to scale linearly on massive manycore systems [12], [14], [26], [34], [82] via dataflow computation. However, due to the ever increasing size of AI models, computationally-intensive applications such as Neural Networks are moving towards sparse data structures like graphs, which present communication challenges [71].

Recently, several works have proposed task-based parallelization schemes that accelerate graph and sparse data structure traversal by splitting the program at irregular memory access [17], [56], [60], offering a promising path for parallelizing these communication- and data-intensive applications. Dalorex [60] proposes a data-local execution model that minimizes data movement by operating data where it resides, which shows scaling up to thousands of PUs on a single chip.

In Dalorex, data arrays are scattered across the processing tiles as equal-sized chunks. A tile comprises a PU, a router, and SRAM. Each PU can only access its fraction of the dataset, i.e., there is a single data owner. Because of that, a program

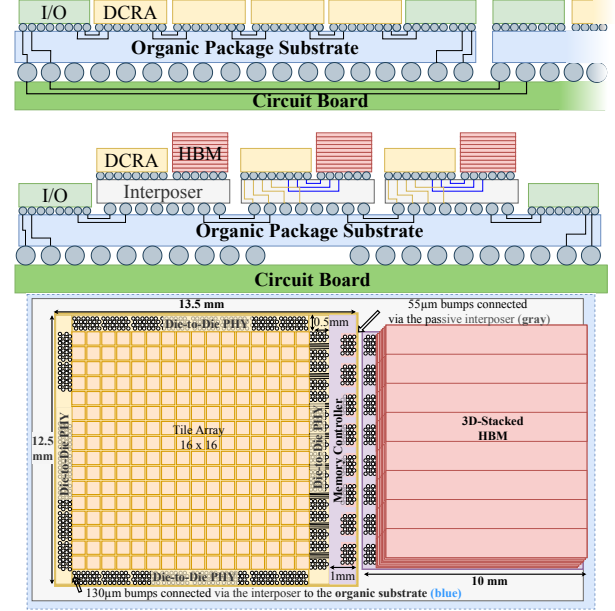


Fig. 1. Two configurations of the DCRA architecture: (top) two packages on a board, each featuring only DCRA chiplet dies, which optimizes for time-to-solution as it aims to parallelize a dataset much as possible (lower data footprint per die); and (bottom) a single package with DCRA dies and stacked DRAM for extended memory capacity, optimizes for performance-per-watt/\$. (Insights based on evaluation results.)

must be split at each indirect memory access to create a tasks executed at the tiles containing the data to be operated on.

While Dalorex introduced a promising new execution model for parallelizing sparse applications, it has several **limitations**: (1) Due to the irregular nature of the sparse data structure, the destination tile may be anywhere on the tile grid. As a result, as the number of tiles in the system increases, so does the average distance of communication for task invocations, adding **network contention**. (2) Because the data footprint per tile shrinks when parallelizing across more tiles, the likelihood that a tile will own much hotter data than others increases. The fact that an operation must be done by the data owner leads to a growing **work imbalance** when scaling out. (3) Dalorex assumes a homogeneous, arbitrarily large grid of processing tiles. It **does not address how to fabricate such large tile grid** in a cost-effective manner, nor how to communicate fine-grain task messages efficiently across multiple chips.

Our work overcomes the above limitations by: (a) introducing proxy regions of tiles with copies of data to reduce task invocation distance and work imbalance; (b) designing a scalable system where chip packages are composed of an arbitrary number of Data-Centric Reconfigurable Array (DRCA) chiplets; and (c) providing a detailed study of tradeoffs in cost,

performance and energy-efficiency of packaging-time design decisions. We evaluate strong scaling performance when parallelizing sparse applications with up to one million processors without resorting to dataset preprocessing or partitioning.

Proxy Regions: To reduce long-distance communication, DCRA divides the tile grid (configured to run a program) into subgrids. In each subgrid, proxy tiles are assigned to data that resides outside the subgrid. Tasks requiring long-distance communication are first sent to a regional proxy tile. This results in filtering out unnecessary requests to the data owner and significantly reduces the average communication distance of task invocations (see Section V). This approach also improves work balance as a tile that owns very hot data does not need to process all the tasks that access it. We demonstrate the benefits of this for the task responsible for vertex-update in graph applications and the reduction phase of sparse linear algebra and histogram.

Reconfigurable Architecture: While Dalorex studied that performance and energy efficiency of task-based execution with different granularity of SRAM per tile, a specific size is decided for tapeout. When we factor in the fabrication cost of such data-local architecture, we found that this granularity also affects key metrics of throughput or energy efficiency per dollar. Because fabricating different silicon masks for different target metrics is prohibitively expensive, we propose composable architecture where crucial decisions like on-chip memory capacity or off-chip bandwidth are taken post-silicon (during chip packaging). Figure 1 depicts two packaging alternatives where the same DCRA dies (also referred to as chiplets) are integrated to create different chip products, each optimized for a different metric. A DCRA die may be attached at packaging time to a DRAM device. This effectively increases the capacity of a tile’s *local memory* since the DRAM storage is logically partitioned across the tiles of the adjacent DCRA die.

The technical contributions of this paper are:

- Software-reconfigurable proxy regions that removes the limitation of data-local architectures that a data operation can only be done by data owner. This reduces distant communication of tasks and improves work balance.
- A scalable architecture where chip design decisions such as on-chip memory, number of PUs, network topology and off-chip bandwidth are taken post-silicon.
- A practical path for manufacturing chip packages by composing DCRA dies. The first design that proposes interleaving any number of compute and DRAM chiplets.
- A detailed study of tradeoffs in cost, performance and energy-efficiency of several package designs.

We evaluate DCRA and demonstrate that:

- The proposed proxy regions reduces network traffic by $1.8\times$ over a prior data-local architecture [60].
- Optimized task scheduling and buffering can improve the overall system’s throughput up to $5\times$.
- Different packaging options of DCRA leads to different optimal design points for key metrics in HPC, such as energy-efficiency/cost or throughput.

TABLE I
POST-SILICON DECIDABLE MEMORY CAPACITY, # OF PROCESSING ELEMENTS, NETWORK TOPOLOGY PER CHIP PACKAGE, AND WHETHER THE PROCESSING ELEMENTS CAN EXECUTE INSTRUCTIONS.

Reconfigurable Aspects / Prior Work	Memory Capacity on package	#Processing Elements on package	Configurable Network Topology	Software ISA Programmable Processors
Tesseract [3]	✓	✗	✗	✓
GraphQ [96]	✓	✗	✗	✓
Fifer [21]	✓	✗	✗	✗
Dalorex [60]	✗	✗	✗	✓
PolyGraph [17]	✓	✗	✗	✗
Piton+Maple [7], [59]	✗	✗	✗	✓
ESP [11], [24]	✗	✗	✗	✓
Manticore [92]	✓	✗	✗	✓
Graphcore [37]	✗	✗	✓	✓
Sambanova [20]	✓	✓	✓	✗
Cerebras [12]	✗	✗	✓	✓
Groq [26]	✗	✗	✗	✓
Tesla Dojo [26]	✓	✓	✗	✓
Esperanto [21]	✗	✗	✗	✓
Google TPU [34]	✓	✗	✓	✗
Nvidia A100 [14]	✓	✗	✗	✓
DCRA	✓	✓	✓	✓

- It is possible to construct a data-centric execution model exhibiting strong scaling performance upto a million PUs.
- Our BFS parallelization is $3.8\times$ faster than the most performant entry of the Graph500 list for RMAT-26.

II. BACKGROUND AND MOTIVATION

Graph and sparse linear algebra applications do not exhibit spatial nor temporal locality, resulting in poor cache behavior and intense traffic in the memory hierarchy [48].

Prior work aiming to accelerate these workloads mitigate memory latency via decoupling, prefetching, and hardware pipelining techniques [1], [17], [27], [55], [56], [59], [62], [70], [81]. Fifer [56] and Polygraph [17] also increase utilization through spatiotemporal parallelization. However, all of these works store the dataset on off-chip DRAM; thus, their scalability is limited by the network and memory bandwidth. Tesseract [3] and GraphQ [96] tackle this problem via processing-in-memory. However, their proposed integration of PUs on the logic layer of a memory cube [67] is less scalable than the manycore integration proposed by Dalorex [60].

Section II-A reviews the latest manycore architectures with a focus on chip manufacturing. Section II-B details the data-local execution model of Dalorex, since this paper builds on top of it to improve work balance and network contention, as well as to design a more practical system integration.

A. Modern Manycore Systems and Chip Fabrication Cost

In recent years, the widespread demand for large deep-learning models has accelerated the development of manycore and dataflow systems that can massively parallelize compute-intensive workloads. Although the demand for graph and sparse linear algebra workloads is growing, we have not seen systems exhibiting as high strong scaling performance as dense systems. This is due to the irregularity of the data-access patterns and the high memory-footprint-to-compute ratio.

Table I shows a selection of the manycore systems published over the last five years, where the upper ones focus on sparse workloads and the rest focus on AI. While some of these large manycores have good attributes for sparse data processing (large on-chip SRAM capacity [12], [26], [37], [60], [82] or on-package DRAM [3], [14], [20], [34], [92]), the ratio of memory capacity and PUs is optimized for dense computation, and the interconnect is designed for dataflow communication. For our work, instead of designing a manycore architecture with a memory-to-PU ratio and network optimized for sparse data, we propose a chiplet architecture where these can be configured at the packaging time.

Big players in the semiconductor industry have moved towards having multiple dies in a chip package [4], [25], [44], [54], [80] to reduce fabrication cost and enable reusing components across different products. From the silicon manufacturing perspective, the Non-Recurring-Engineering cost (NRE) of a wafer mask is so high with respect to the silicon wafer itself that the cost per wafer is $18\times$ larger when manufacturing 100 wafers, instead of 100,000 [33]. Since the volume of silicon production of each chip architecture generation is not as high in the HPC market than in the consumer electronic market, we argue that mass fabrication of a chiplet that can serve as a building block for scalable architectures is a valuable proposition. That is why we design a unique chiplet, which can be fabricated in high volume to amortize NRE costs, and then integrated into a Multi-Chip Module (MCM) package with a smaller or larger grid of dies. As depicted in Figure 1, our design optionally integrates DRAM dies between columns of DCRA dies (and not just on the borders as current designs).

B. The Data-Local Execution Model

In our task-based model, the original program is split into tasks that are executed at the tile co-located with the memory region that the task operates on. A task with dependent tasks can spawn them by injecting inputs for each task in the output queue (OQ), which drains into a logical network channel (one per task type). The entire program is executed as a sequence of tasks, with no concept of execution threads (no main task). The parallelization level is determined by the number of tiles with tasks ready to execute, i.e., waiting on an input queue (IQ). There is one IQ per task type. An IQ is populated with invocation parameters created by either a prior task executed in the local tile or by incoming task messages at the network channels. While some spawned tasks are likely to be in the nearby tiles due to data placement policy, for others, the destination may be anywhere at random in the tile grid. As the size of the grid increases, so would the average number of router hops of a task invocation.

Tile Grid and Network Routing: The grid's size, hence the number of tiles a program is to run on, is determined by the user at compilation time. The logical tile ID is set by the microcode when a workload is selected to run on a grid, and it is used for XY routing. Since the dataset is statically partitioned across the tiles on the grid, and the first parameter of a task message is a global index to a data array, this

index is used to route the message, avoiding message headers altogether. Based on the size of the array associated with each logical NoC for routing purposes, the router selects the bits that indicate destination tile ID.

Task Prioritization: In Dalorex, work efficiency and PU utilization highly depend on the order of task executions. In order to make task invocations non-blocking and non-interrupting, the inputs for tasks arrive at a tile's task-specific queues through a unit called Task Scheduling Unit (TSU). TSU's main role is to determine the order of execution of tasks based on occupancy of queues. Priority is given to tasks whose IQ is highly populated, or OQ is empty. This allows the tile to sense the network pressure and execute tasks that will relieve pressure when it is high (IQs are full) or increase when it is low (OQs are rarely pushing).

DCRA has reconfigurable queue sizes, and we analyze the impact of queue sizes on performance for different applications in Section V-A. Section V-B also shows how our proxy regions reduce the excessive traffic that appears with large tile grids.

III. DCRA: A RECONFIGURABLE TILED ARCHITECTURE

In this section, we describe how DCRA overcomes the network scalability challenges through its *software reconfigurable* mechanism, such as proxy regions, queues, scheduling, and caches. We also introduce our *package-time reconfigurable* design and provide a thorough analysis of cost versus performance of various manufacturing options.

A. Reducing Network Contention by using Proxy Regions

In DCRA, dataset arrays are scattered as equal-sized chunks to tiles, where each tile *owns* a chunk of each data array, similar to Dalorex. In addition, DCRA introduces proxy ownership for tiles other than the owner by temporarily storing some remote data. We first define *proxy regions* by subdividing the tile grid. We distribute the proxy ownership for a select data array across the tiles of each proxy region such that the most recent updates coming from within region can be stored inside the local proxy tile before being sent to the true owner. The purpose of proxy regions is twofold: it reduces network contention by reducing the average number of hops between task invocations and smooths out workload imbalance by allowing tiles other than the data owner to execute tasks. Figure 2 explains how proxy regions are configured in software and depicts how regional tiles executing proxy tasks reduce long-distance communication.

Applicability: Each proxy region is responsible for the entirety of a dataset array. Any task in the data-local execution model can have a proxy task. However, it is more beneficial to have proxy for tasks whose owner tile can be anywhere in the tile grid. This is the case of the vertex update in graph applications and the reduction phase of sparse linear algebra and histogram, which we evaluate in Section V. Proxy tasks could be applied to read-only data, as well as for modifiable arrays. For the latter, the proxy updates need to be propagated to the owner at some moment.

```

param VERTICES_PER_TILE = 10 #64 tiles, total of 640 vertices
param PROXY_REGIONS = 4 #The more regions, the larger the proxy array
var P_DIST[NODES_PER_CHUNK*PROXY_REGIONS] #The proxy array
var DIST[NODES_PER_CHUNK]
OQ2 = channel(target=T3', encode=VERTICES_PER_TILE, proxy_x=4, proxy_y=4)
OQ3 = channel(target=T3, encode=VERTICES_PER_TILE)

```

```

task T2 (neigh_b,neigh_e,node_dist)
for i in range(neigh_b, neigh_e):
  OQ2 = EDGES[i].neigh_idx (=531)
  OQ2 = node_dist + EDGES[i].val

task T3' (neigh_id, new_dist):
if (new_dist < P_DIST[neigh_id]):
  P_DIST[neigh_id] = new_dist
  OQ3 = neigh_id
  OQ3 = new_dist

task T3 (neigh_id, new_dist):
if (new_dist < DIST[neigh_id]):
  DIST[neigh_id] = new_dist
  add_to_frontier(neigh_id)

```

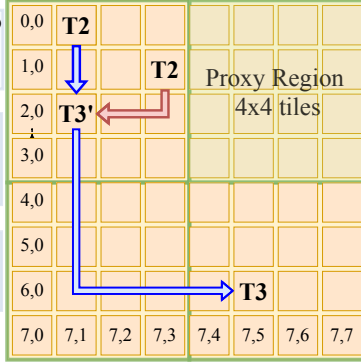


Fig. 2. Software configuration of proxy regions and flow of tasks for single-source shortest path (SSSP). Based on the number of configured proxy regions P , the grid is divided into P subgrids, where each region is responsible for a copy of a data array. Each tile is a proxy for a P chunks of the data array (P_DIST). Contrary to Dalorex, T2 does not invoke T3 directly, but instead, its output queue (OQ2) is configured to route to the corresponding proxy tile within the same subgrid. The data owner tile is calculated as $neigh_id / vertices_per_chunk$, which is tile 53 ($y=6, x=5$) in the code example. When a channel is configured as proxy, the proxy tile is calculated doing modulo with the dimensions of the proxy. The red arrow shows an invocation of T3' (the proxy task) for which proxy value was smaller than the received one (new_dist); thus, no message is sent to the owner. The blue arrows show a path for which the proxy value was not minimal, so a T3 invocation is sent to the owner to determine the new minimal value.

Proxy Coherence: Parallel applications often require atomic updates to array elements because any interleaving of parallel executions can occur, including those operating on stale data. This is the case for the Bulk-Synchronous Parallel (BSP) model for graph applications, where the updates must only be made visible at the end of each epoch (ending with a barrier). Moreover, in BSP and most parallel formulations, the atomic updates are commutative, so the order of updates does not matter. We leverage these properties to reduce the number of tasks executed on the owner tile. The reduction is twofold: updates are not always successful (e.g., minimization in SSSP example), and several updates can be merged before being sent to the owner. In our design, proxy updates are propagated to the owner as either write-through (every time the value changes) or write-back (when proxy data gets invalidated). These policies are independent of the fact that proxy data can be cached (Section III-C), although caching influences how often the data gets invalidated.

Application-specific Proxy configuration: In this paper, we evaluate one application (Pagerank) following the BSP model, for which updates are propagated to the owner at the end of each epoch. This is done by invalidating the write-back proxy and giving all elements a default value. A similar strategy is used for Histogram and SPMV, whose additive updates only need to be accumulated at the end of the execution. For the SSSP example shown in Figure 2 and the other applications described in Section IV, the code explicitly performs write-through updates. This is because our SSSP implementation does not use barriers between epochs; thus, updates should propagate quickly to avoid stale data.

B. Software Configurable Queues to Optimize Throughput

DCRA offers more software-reconfigurable features that are tuned for different applications and tasks (Table II). This section describes configurations for task scheduling, queue sizes, NoCs, SRAM, and prefetching, and summarizes the rest.

Task Scheduling and Queue Sizes: To mitigate back-pressure from end-point routers, input queues must have a sufficient size to buffer message bursts. These bursts naturally happen in sparse linear algebra when a column of a sparse matrix is much denser than the rest or in graph traversal when a vertex has many more neighbors. However, making queues too large has unwanted side effects, such as message waiting very long on average to be processed (leading to data staleness). Moreover, in data-local execution, there is no global orchestration of tasks, so task scheduling depends solely on information that is local to each tile. Thus, queue occupancy and back-pressure help signal tiles to adapt their task scheduling to prioritize tasks that would lead to higher overall utilization, effectively resulting in a Goldilocks effect. We study the size ratio between IQs and OQs on performance in Section V-A. For the rest of the evaluation, we choose a ratio between IQ and OQ size proportional to the expected average number of hops in that channel because in a 2D network, the more hops, the more contention under irregular communication, and so more input buffering is needed to maintain throughput. For *proxy tasks* we set the ratio to width of proxy subgrid, while for *main tasks*, we set this ratio proportional to the width of the tile grid. However, as we observe later from the queue characterization of Section V-A, different applications behave different with regard to buffering, which is related to application sensitivity to data staleness. Since this sensitivity depends on the synchronization point (barriers or epochs), we envision that queue size could be set differently based on the workloads by a compiler via static analysis. Based on this and the communication distance between tasks, the compiler can more adequately set the queue sizes for different tasks. This can also help utilize the storage better and give more SRAM to the caches.

NoC Reconfigurability: In a DCRA system, there are P physical NoCs and C logical channels. These channels can be assigned to different physical NoCs, or to the same one. If they are in separate NoCs, these messages are routed uncontested. If they are in the same NoC, they are routed in a round-robin fashion. If the application is not using all of the available NoCs, a task can use more than one channel increase the communication bandwidth with the task being invoked. The allocation of physical to logical resources is fully reconfigurable, a NoC can be used by multiple tasks, and a task can use multiple NoCs.

C. Software Configurable Caches using the local SRAM

In a DCRA system, the SRAM in each tile can be used either as a scratchpad or as a cache [15], [16], [38]. The cache mode stores cacheline tags in SRAM, including a valid bit. To minimize the hardware and energy overhead of using the SRAM as a cache, we make the caches directly mapped.

TABLE II
RECONFIGURABLE PARAMETERS OF DCRA

Tapeout-time Design Decisions
of Tiles per die
SRAM per-tile (MiB)
#Physical NoCs and Width of each one (in bytes)
Max.# of Router Buffer Entries per Physical NoC
Max.# of Logical NoC Channels per Physical NoC
Max.# of Memory Controller Channels per DCRA die
Packaging-time Design Decisions
of DCRA dies per package
of DRAM dies per package and capacity of each (GiB)
Ratio of DCRA-DRAM dictates Mem. BW and Capacity per DCRA
of I/O dies per package (Off-Package BW)
Compile Time Configurations
Size and Place of the grid that the workload uses (grid of dies)
Whether the dataset uses SRAM as a scratchpad or D\$
Size of the D\$ (in data elements)
Mapping of Tasks to Logical NoC Channels
Mapping of NoC Channels to Physical NoCs
Number of Router Buffer Entries of each NoC Channel (shared pool)
Arbitration ratio between Channels sharing a Physical NoC
Per Task
Whether a Task has a Proxy and the size of the Proxy region
Whether the Proxy array is cached or kept in full
Whether Proxy updates are propagated write-through or write-back
Whether a Task uses data prefetching during execution (if dataset is cached)
Size of the Input Queue (IQ)
Size of the Output Queue (OQ) if the Task produces into a NoC Channel

This cache mode is used to configure the *proxy cache* (P\$), which holds proxy data, and the *data cache* (D\$), which caches the dataset arrays when the package has integrated HBM. When scaling out the parallelization of a dataset, if the memory footprint per tile is so low that everything fits in the local SRAM, the D\$ would not be configured, and the PUs would access the data arrays as a scratchpad. (Both the memory controller and the HBM would be switched off).

The D\$ and the P\$ have reconfigurable sizes. Only one D\$ can be configured, and its line width equals the bitline width of the DRAM memory controller (512 bits in our experiments with HBM). Every proxy task would configure its own logical P\$, although they all use the same hardware comparison logic. This is necessary because writing back proxy data requires knowing which task to send it to.

D\$ misses and evictions: Upon a miss, the D\$ fetches the full cacheline from DRAM without checking for coherence because the data is not shared across tiles. This fetch uses a physical address since each DRAM module is private to each DCRA die with 1-1 exclusive mapping between each tile and DRAM vault. Therefore, each tile's local SRAM is backed up by a DRAM storage of size $DRAM_capacity/tiles_per_die$. The details of the DRAM assumed for the evaluation are described in Table III. The D\$ has a write-back policy and a dirty bit per line, so when modified data get evicted, it is written back to DRAM. Since the D\$ of each tile only contains the part of the dataset that the tile is responsible for, there is no coherence issues for modified data.

P\$ misses and evictions: A miss in the P\$ returns a default pre-configured value such as 0 for Histogram or infinite for

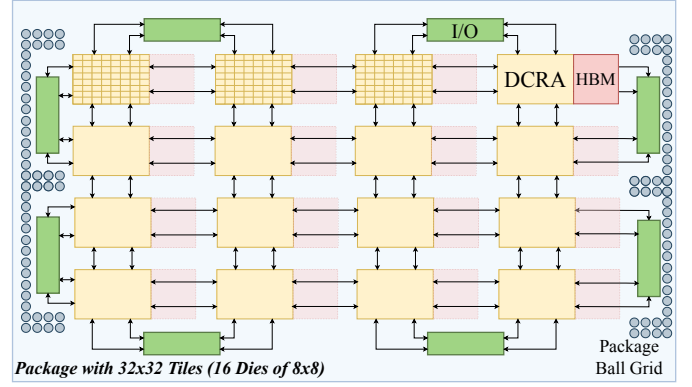


Fig. 3. Top view of an example chip package with 32x32 tiles. The number of DCRA dies would determine the compute capacity, while including HBM dies would determine the compute-to-memory ratio of the chip architecture. The number and sizes of the I/O dies would determine the provisioned off-chip bandwidth.

SSSP. A P\$ is either write-through or write-back, depending on how the proxy region is configured for that task. On eviction, the data is simply replaced with write-through, while with write-back, an update task is sent to the owner. Since the intention of the P\$ is to coalesce updates, all lines are considered dirty in the write-back mode. By the end of a kernel, the write-back mode should evict all P\$ lines to merge the updates before outputting the result. To overlap the data merge, we include a heuristic in the TSU to flush the P\$ when all queues and network buffers are empty. In our experiments, a P\$ line contains a single data element to avoid sending multi-update messages in the write-back mode. However, multiple elements per cacheline would increase effective P\$ size, as less SRAM storage is used for tags.

Prefetching The PU has a very simple in-order pipeline, which stalls waiting for data on a D\$ miss. Since the first parameter of every task message contains an array index, and the TSU knows to which array it corresponds (as it is necessary for network routing), we use this information to prefetch the data. A task may access more than one array using the same index. Thus, we add another pointer to the TSU's task configuration table so that the TSU prefetches both, if needed. The task entries in that table also have an extra bit saying whether the PU prefetch data during the execution of the task. Tasks can only access data within their dataset chunk, and when a task accesses more than one array element, it often does so with a streaming pattern. To prefetch those accesses, we enable the PU's next-line prefetcher (stride=1) for tasks that access more than one element.

D. Package reconfigurability

Whether to integrate HBM on the chip is a package-time decision based on the target metrics of the final product. Figure 3 exemplifies how the DCRA dies could be packaged to provide high memory capacity per processor.

Extensible Memory Capacity: HBM capacity can be increased by either stacking more DRAM layers or having larger layers. In our evaluation, we assumed a 10x11mm 4-

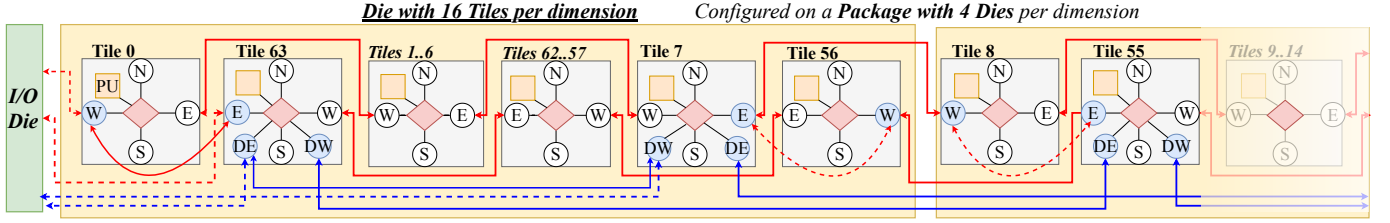


Fig. 4. Links between horizontal tiles within a DCRA die and across dies. The red links show the network that connects every tile (**tile network**), while the blue links represent a network that only connects to one tile per die (**die network**). Because of the die network, the tiles at the edges of a die have radix-9 routers, while the rest have radix-5 routers. The ports shadowed in blue are reconfigurable, i.e., we can select which link to use at runtime. These enable re-configuring any subgrid within the system to become Torus. The die placed at the end of a package will interface with the I/O die. All four links at the edge can be connected to the I/O die when loading the program and the dataset to maximize the I/O bandwidth. During the program execution, both networks can become torus, or we can have the tile network as a torus and the die network as a mesh, to keep streaming data coming from outside the package. Moreover, if the grid in which a program runs spans several packages, the ports can be connected to conform a torus across packages as well.

layer HBM die (up to 16 layers has been demonstrated [65]). DCRA could also integrate larger HBM dies, provided that the distance between DCRA dies remain within 25mm (limit of common PHYs for MCM [5], [58], [73]). Selecting the amount of DRAM attached to a DCRA die depends on what level of parallelism is expected on a final product. If the chip is always expected to parallelize a dataset to the limit of strong scaling, HBM might not be necessary. In contrast, with target metrics like performance-per-watt, larger on-package memory capacity is essential. We evaluate both options in Section 9 and discuss the tradeoffs.

Integrating the HBM dies: Figure 1 depicts the connection between the DCRA and the HBM die via a silicon interposer. Although we think that a silicon bridge [47] or substrate integration (given enough layers) [4], [39] might be possible, we assume the interposer integration in our evaluation because it has been demonstrated to work in real products [14], [54]. Another alternative is 3D integration, where the HBM die is placed on top DCRA. We evaluate this in Section IV-C to understand whether the advantages are worth the power, thermal and integration challenge [9], [29].

Designing the network: When dealing with irregular network traffic in dimension-ordered routing (DOR), a 2D-torus provides a more uniform utilization than a 2D-mesh [60]. DOR keeps the router logic simple, and deadlocks are avoided using bubble routing [69]. To make implementation practical on 2D silicon, the 2D-torus is folded: a set of links connects the even-numbered tiles, and the other set of links connects the odd-numbered ones. The torus can be arbitrarily large, i.e., be confined within a die or span multiple dies, packages, or boards. Table III presents the interconnect energy and latency assumed for our evaluation at each level. Figure 4 shows that the routers at the edges of each die can be configured to connect to a router on the next die or wrap around by connecting to the adjacent tile (Tiles 0 and 63).

Reconfigurable topology: We can reconfigure a 2D-torus interconnect to become two 2D-mesh networks by not connecting the wrap-around links on the routers at the edges. Utilizing two 2D-meshes may be the right choice when running a workload with near-neighbor communication [6]. As Figure 4 shows, DCRA has two hierarchical networks that route per tile and per die. Each network topology is individually configured. While bringing the data inside the package from disk, they

both would be configured as a mesh to enable data streaming from the I/O dies. During the execution, both may become torus, or the per-die network can remain open to I/O data.

Off-Chip Bandwidth: DCRA delegates the design of the interconnect between packages to the I/O chiplets. This allows DCRA dies to remain agnostic to the specific protocol (e.g., PCIe 6.0 [72]). It also delays choices like off-chip bandwidth to packaging time, which are taken based on the requirements of the final product. The off-chip bandwidth could be up to the bandwidth of the I/O-DCRA interface. Figure 4 shows a configuration where two 32-bit bidirectional Torus networks interface each border tile on a die (16 tiles per side). Considering that only one side of the die interfaces with the I/O chiplet, the border die can deliver up to 512GB/s. Multiplying that for the number of bordering dies on a package would determine the maximum off-chip bandwidth.

What decides the package size? A package is as big as the size of its substrate. A silicon substrate typically scales 2-3x the reticle size, but this could technically scale up to a wafer-scale interposer [64]. On a Multi-chip Module (MCM) integration, server-class chip packages typically span over $4500mm^2$ [4], [53], [54]. However, MCM substrates have been fabricated to nearly $100,000mm^2$ [22], [82]. So the choice of the package size may be determined by the unit of sale rather than a constraint in the substrate size. Regarding the number of dies on a package, although we see chip packages with tens of them [25], bonding may set feasibility bound. The package yield is determined by the bonding yield of each die. [83]. When using DCRA dies of 16x16 tiles, the practical limit may be 128x128 tiles per package (64 dies). In our evaluation, we set the package size to 64x64 tiles, i.e., $4780mm^2$, which is in line with the size of server-class chips.

Scaling beyond a package: Off-chip network topology and bandwidth are determined by the I/O chiplets selected. The I/O links across packages could also be electrical or optical [19], [50]. If a system featuring DCRA chiplets is expected to have near-neighbor communication, several packages are connected on a board using a 2D network with electrical links. However, when irregular or all-to-all traffic is expected, it would be beneficial to connect packages directly with optical links on a high-dimensional network [2], [8]. For simplicity, we assume electrical links between packages DCRA in our evaluation.

Graph Partitioning is commonly used in distributed graph

processing [84] to reduce communication. In addition to using proxies, graph partitioning can also be used during data placement in DCRA so that each subgrid would store a graph partition with fewer cross-partition connections.

IV. EVALUATION

Applications: We evaluate the performance of DCRA on four graph workloads, one sparse linear algebra, and a histogram benchmark [79] to demonstrate the generality of our approach for memory-intensive applications.

Breadth-First Search (BFS) determines the number of hops from a root vertex to all vertices reachable from it; *Single-Source Shortest Path (SSSP)* finds the shortest path from the root to each reachable vertex; *PageRank* ranks websites based on the potential flow of users to each page [40]; *Weakly Connected Components (WCC)* finds and labels each set of vertices reachable from one to all others in at least one direction (using graph coloring [75]); *Sparse Matrix-Vector Multiplication (SPMV)* multiplies a sparse matrix with a dense vector. *Histogram (Histo)* counts the number of values that fall within a series of intervals. We perform the evaluation using real-world networks and synthetic datasets. We use several different sizes of synthetic RMAT graphs [43] of up to 67M vertices (V) and 1.3B edges (E), with up to 12GB of memory footprint, as well as real-world graphs Wikipedia ($V=4.2M$, $E=101M$). For Histogram we use the same datasets and have E elements to be filtered into $V/8$ bins (as values, we use the edge array index plus its value, modulo the #bins)

Methodology: We build upon the cycle-level simulator of Dalorex [60] and extend it to support data and proxy caches, an HBM model, and three levels of network interconnect (between tiles, dies, and packages). Table III summarizes our additions to the energy, latency and area model for network links and memory technology. In addition to the latency of the links shown in Table III, the simulator models cycle-accurate network congestion (it evaluates the routers every clock cycle). We use the existing model on the simulator for the power and area of the cores and routers. This is modeled based on characterizations of manycore architectures [18], [49], [61], [90], [91], [93], and transistor scaling to a 7nm process [77], [88]. We assume a 1GHz frequency for the die logic.

A. Characterizations

We have experimented with the DCRA configuration knobs listed in Table II. Section V-A characterizes several sizes of task queues and proxy grids, as well as four network options. Section V-C studies the cost-effectiveness of integrating HBM dies in performance and energy efficiency. Due to space considerations, for the rest of the experiments, we verbally present our insights here.

SRAM size: We experimented with SRAM sizes ranging from 128KiB to 4MiB and found 1.5MiB of SRAM per tile to be enough to hold the program code, the task queues, and a well-performing size of D\$ and P\$. The P\$ saves on-die traffic on the task for which it is enabled, reducing the average number of router hops for that task. The ideal size of the P\$ depends on the ratio between the program grid and the

proxy grid. The D\$ saves traffic to the HBM device, reducing memory-controller contention and energy. An appropriate size of D\$ yields a hit rate that is high enough not to saturate the memory channels when the processing units are fully utilized. These sizes are compile-time configurable, as mentioned in Section III-B. At 1.5MiB, the tile area dedicated to SRAM is $7\times$ larger than the area of the router, PU and TSU together. Since DCRA is focused on Data-Centric computing, this size is a good tradeoff.

Die size: All our results use dies with 16×16 tiles. This size is practical for several reasons: (a) it matches common sizes of HBM chiplets [42], [57], [65]; (b) it allows for larger configurations per package, as the packaging yield depends on the number of dies; (c) the lower yield of a 32×32 -tile (27×25 mm) die results in getting 62% less good dies per wafer [31]. Larger dies would achieve a high yield with the overhead of adding tile redundancy [37], [45]. However, we find it appealing to have a unit die that is small enough to add flexibility at packaging time.

Network interconnect: We use one die network and two torus networks for all results but the characterization Figure 6. Both torus networks use 32-bit links across dies, but one them uses 64-bit links inside the die. We used this configuration due to its good performance-to-cost ratio. The interconnect bandwidth between DCRA dies is sufficiently low (~ 800 Gbit/s/mm) to avoid an expensive silicon interposer (which can reach up to 5Tbit/s/mm [58], [73], [87]). For the die-to-die substrate wires, we assume a BoW-128 PHY with $130\mu\text{m}$ bumps [5], [58]. To connect DCRA and HBM, we assume a 65nm CMOS passive interposer [13], [68] with $55\mu\text{m}$ bumps [58].

B. Cost Model

Die Cost: For silicon, we assume that a 300mm diameter wafer featuring 7nm transistors costs \$6,047 [33]. We obtain the cost per die by dividing the wafer cost by the number of good dies per wafer. This was obtained with a die yield calculator using Murphy’s model [31], using 0.2mm scribes, 4mm edge loss, and 0.07 defects per mm^2 . When comparing cost-effectiveness in Figure 9, we do not include the Non-Recurring Engineering (NRE) cost of the DCRA dies since all the alternatives use the same chiplets.

Packaging Cost: All our results featuring grid sizes over 64×64 use multiple chip packages (of 64×64 tiles each, based on our rationale from Section III-D). Although costs of packaging and die bonding are not disclosed, there is public information on the cost overhead with respect to the cost of the die. We assume the cost of the 65nm silicon interposer connecting a DCRA die with HBM (including bonding) to be 20% of the price of a DCRA die [83]. We assume the cost of an organic substrate to be 10% of the price of an equal-sized DCRA die, and the bonding adds an additional 5% overhead [41], [78].

HBM Cost: We assume an 8GB HBM2E device with eight 64GB/s memory channels. While this cost is not disclosed, we made an educated guess using public sources [33], [66] and

TABLE III
ENERGY, BANDWIDTH AND LATENCY ASSUMED FOR THE EVALUATION

Memory Model Parameters	Values
SRAM Density	3.5 MiB/mm ² [89]
SRAM R/W Latency & Energy	0.82ns & 0.18 / 0.28 pJ/bit [89]
Cache Tag Read & Compare Energy	6.3 pJ [89], [90]
HBM2E 4-high Density	8GiB/110mm ² (74.5 MiB/mm ²) [42]
Mem.Channels & Bandwidth	8 x 64 GB/s [42]
Mem.Ctrl-to-HBM RW Lat. & Energy	50ns & 3.7pJ/bit [35], [63]
Bitline Refresh Period & Energy	32ms & 0.22pJ/bit [23], [76]
Wire & Link Model Parameters	Values
MCM PHY Areal Density	690 Gbits/mm ² [5]
MCM PHY Beachfront Density	880 Gbits/mm [5]
Si. Interposer PHY Areal Density	1070 Gbits/mm ² [5]
Si. Interposer PHY Beachfront Density	1780 Gbits/mm [5]
Die-to-Die Link Lat. & Energy	4ns & 0.55pJ/bit (<25mm) [58]
NoC Wire Latency & Energy	50 ps/mm & 0.15pJ/bit/mm [36]
NoC Router Latency & Energy	500ps & 0.1pJ/bit
I/O Die RX-TX Latency	20ns [72]
Off-Package Link Energy	1.17pJ/bit (80mm) [87]

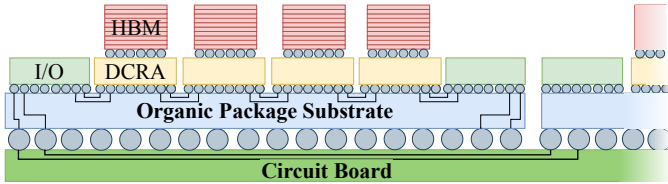


Fig. 5. Alternative packaging of an HBM device on top of a DCRA die. The design of the DCRA die would need to be different; it would behave as a very active interposer. This would require making the DCRA die larger to accommodate the links and power supply pads below the HBM device.

other technical blogs. We assume a 7.5\$/GB of HBM. This is much more affordable than when HBM was released in 2017, and we expect this price to decrease over time as more vendors fabricate HBM [42], [51], [57].

C. 3D Integrations

Prior work [3], [36], [94], [96] has assumed 3D integrations where processing cores are on the base plane of the 3D-stacked memory, accessing the TSVs directly. However, we believe this may be impractical. There are very few foundries that can fabricate HBM technology, and the design seems to only change with every generation of JEDEC specification [32] (e.g., HBM2, HBM2e, HBM3) which vendors conform to. So it would be expensive (if possible) to get a foundry to fabricate an HBM die with a custom base layer. Moreover, the base layer of the HBM stacks is filled with MBIST logic and PHY [28], [42], [57], [65]. Vertical stacking would reduce HBM latency, but more importantly, it would significantly reduce wire energy [36]. Having HBM on top of a compute die is challenging for bonding, power delivery, and thermal dissipation [95]. It seems more practical to use an off-the-shelf HBM die and integrate it via an interposer. We observe two alternatives: (a) having the HBM die adjacent to a compute die and connecting them via a passive interposer, or (b) having the HBM die on top of the compute die, which would behave as a beefy, active interposer [78], [85]. The most common integrations of HBM with compute dies are horizontal [4], [30], [47], [53], [54], [87], [92], where we have only found one vertical integration of memory but using SRAM [80]. Since

the power-density of the DCRA die is very low due to the large area dedicated to SRAM, we think that integration like the one depicted in Figure 5 is not out of the question which we consider in Section V-C.

D. Comparison with the State-of-the-Art

Since we want to understand where our system stands with respect to the Graph 500 list [52], we adhere to their guidelines. Graph500 requires timing separately the reading, preparing, and loading of the graph onto the system and the graph traversal itself. In our case, we do not perform any dataset pre-processing and directly read the CSR structure from disk. The time for loading the dataset depends on how many disks the data is spread across, the speed of these disks, and the off-chip bandwidth. Assuming latter to be the limiting factor, we provide a lower bound by dividing the dataset size by the off-chip I/O.

Since our goal is to evaluate the performance of our architecture, we concentrate on graph traversal. Based on the Graph 500 benchmark guidelines, we begin counting cycles when the search key is loaded onto the system, and we stop counting when the last vertex is visited. We report traversed edges per second as $TEPS = m/time$ where m is the number of edges connected to the vertices in the graph traversal starting from the search key. Due to runtime limitations of our simulator, we only perform one search from the root node and report the TEPS for that search. Because we also evaluate other applications than graph traversal, when we report for SPMV and Histogram, we consider # input elements to process.

V. RESULTS

In this section, we first present the characterization of a crucial *pre-silicon choice*: the number of physical networks and their width. Second, we characterize *software-time* configurations, such as the size of the input queues for tasks concerning the output queues. Third, we explore *packaging choices*, including two with SRAM-only and another two with different integrations of HBM. Later, we show the performance gains over the prior work Dalorex, characterizing the impact of *proxies* on network traffic. Finally, we study strong scaling, performance-per-watt, and performance-per-dollar by parallelizing RMAT-26 for increasing grid sizes, ranging from 256 tiles to 1,048,576 tiles. We compare our fastest results versus entries of the Graph500 ranking [52] and other works [10] for same datasets sizes.

A. Characterizations

Network: We evaluate four different network options to characterize how the intra-die (ID) out-of-die (OD) network bandwidth affects runtime, including: (a) two 32-bit networks whose flow gets throttled to a shared 32-bit when crossing die boundaries; (b) a 32-bit and a 64-bit networks whose flow gets throttled to a shared 32-bit when crossing die boundaries; (c) same as b but with two 32-bit links across dies; (d) same as b but maintaining the bandwidth across dies.

All runs are performed on a single chip package with a 64×64 tile grid across 16 dies. We assign the 64-bit network

to the channel used by the proxy task, while the other tasks use the 32-bit network. The proxy subgrids are of size 16x16, matching the die size. Thus, overall there are 16 subgrids.

Figure 6 (top) shows that the increase in network bandwidth is beneficial for four applications. Figure 6 (bottom) shows the average percent of the runtime that the PUs were executing tasks. One can observe that Histogram and WCC start with higher utilization than other workloads with the lowest bandwidth setting, which may explain why their performance does not improve significantly more with increased bandwidth.

Across the board, the geomean improvement of option (c), with two 32-bit links between dies, is $1.72\times$ geomean faster than option (a). Since this is a tapeout-time parameter, it is essential to understand the cost impact of this choice. The total die area grows by 4.5%, but the performance improvement renders it worth it. For the rest of this section, the results are evaluated using option (c).

Returning to the utilization of Figure 6 (bottom), note that RMAT-22 has 2^{22} vertices, and we are executing it on 2^{12} tiles (a 64×64 grid). This level of parallelization (with little work per PU) makes it challenging to achieve a 100% utilization since the ramp-up time (to get enough tasks in the network) and the cool-down phase (where the last tasks are executed) represent a significant part of the total runtime.

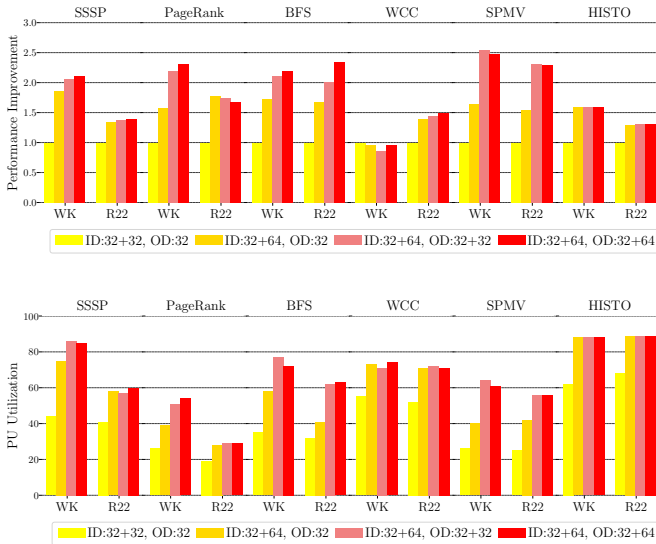


Fig. 6. Performance improvement (top) and PU utilization in % of total runtime (bottom) of three network options with different intra-die (ID) and out-of-die (OD) link widths over a baseline of two 32-bit networks whose flow gets throttled to a shared 32-bit when crossing die boundaries. The legend represents the link widths and whether there is more than one link. The X-axis shows the datasets used for each of the applications evaluated. All runs are performed on a 64×64 tile grid using the RMAT-22 and Wikipedia datasets.

Queue sizes: Figure 7 shows the performance improvement resulting from increasing the size of the input queues (IQs), while keeping the size of the output queues (OQs) fixed. Note that the legend does not indicate the queue size but how many times bigger the IQ is compared to the OQ. We observe that increasing the IQ size has a significant impact on performance. In the case of SSSP, BFS, and WCC, we observe a Goldilocks

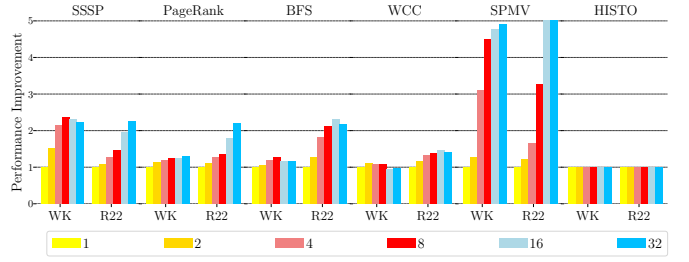


Fig. 7. Performance improvement of growing the input queue (IQ) size while keeping the same output queue (OQ) size, normalized to the baseline of same size IQ and OQ. The legend indicates how many times bigger is the IQ of each task compared to its OQ. The X-axis shows the datasets used for each of the applications evaluated. All runs are performed on a 64×64 tile grid using the RMAT-22 and Wikipedia datasets.

effect. Increasing IQ size improves performance while there exists network contention; once that is removed, larger IQ sizes only increases data staleness. The lack of improvement on WCC and Histogram is attributed to the already high core utilization observed in Figure 6. It is noteworthy that SPMV drastically increases performance due to increased IQ size. Figure 6 used our default IQ-OQ ratio of 8. Figure 7 demonstrates that performance can improve even further, for the case of SPMV, by increasing the IQ ratio. Insufficient IQ size causes end-point contention when bursts of messages arrive, and the PU cannot process them fast enough. A smarter Task scheduler could also help alleviate this problem by dynamically adjusting the IQ sizes among tasks to use the SRAM space more effectively than with static allocation.

B. Comparison with prior work

In order to measure the impact of proxy tasks and re-configurable queue sizes, we reproduce the same configuration as that in Orenes-Vera et al. [60], and compare the performance of DCRA with that of Dalorex.

The advantages of proxy tasks: Figure 8 (top) shows the average number of router hops of a the vertex update message in Dalorex and for DCRA's proxy task. For smaller configurations, the DCRA proxy region is defined as a quarter or the size of the tile grid. For the 128×128 configuration, we use 16 subgrids of size 32×32 for all applications except Pagerank, which uses 64×64 subgrids. These varying sizes help show the impact of the subgrid size on the average number of hops. We can observe from Figure 8 (top) that the proxy region significantly reduces communication, which translates to achieving higher throughput (bottom).

Scalability: Figure 8 (bottom) also shows that DCRA is not limited when scaling to large grid sizes, unlike Dalorex, which starts to plateau after 64×64 due to high network contention. Dalorex gets higher throughput on the 16×16 configuration, since they assume that data footprint per tile always fits on the local SRAM, while DCRA uses a limited 1.5MB SRAM with a backup on HBM.

C. Package Integration Options

Figure 9 evaluates throughput and energy efficiency per unit of cost of three DCRA integrations over Dalorex. We evaluate

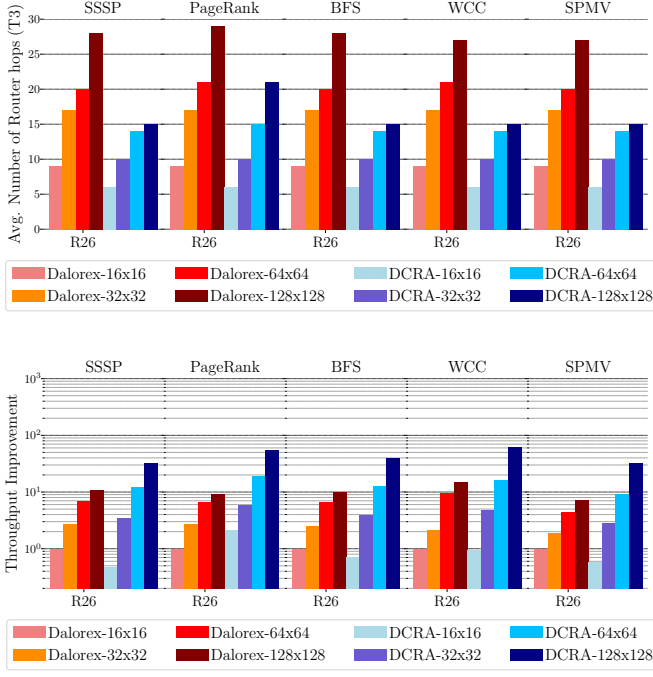


Fig. 8. The top plot shows the average number of router hops per message (lower is better) for the vertex update task. Since DCRA uses a proxy on this task, the average number of hops is smaller. The bottom plot shows the throughput improvement over the baseline Dalorex 16x16 (Y-axis is logarithmic). All the datapoints use the RMAT-26 dataset.

DCRA without HBM dies (only SRAM) and integrating HBM with two packaging options: placing the HBM device vertically on top of the DCRA die (See Figure 5), or horizontally, via a passive interposer (See Figure 1). Since the silicon area of a 64x64 configuration of Dalorex [60] is beyond the reticle limit of 880mm², we assume the same chiplet-based integration of DCRA for Dalorex. This makes their cost very similar (only affected by the interconnect area). Thus, throughput-per-cost differences mostly come from total runtime. We evaluate all integrations on their smallest configuration that fits the dataset. This makes HBM integrations to use a grid size with 16 times less tiles.

Although Figure 9 does not show total throughput, we can observe from Figure 11 (also using RMAT-26) that throughput scales very well. Since DCRA-SRAM does not cost 16 \times more than DCRA-HBM, it wins across the board on throughput-per-dollar. Despite that DCRA-SRAM runs 16 \times faster, it does not consume 16 \times less energy, so DCRA-HBM wins on energy-efficiency-per-dollar.

Note that these results assume a 60\$ 8GB HBM2 die (3 \times more expensive than the base DCRA die in 7nm). This throughput-per-dollar results could change significantly if either HBM becomes cheaper or other DRAM or 3D-stacked SRAM [74] technology (using the same HBM memory controller) becomes cheaper. Considering the two HBM options, our cost model estimated that (should it be practical) the HBM-Vertical integration would cost 5% more than the horizontal one. Therefore, the reason why DCRA-HBM-Vertical wins over the horizontal alternative is because of savings in wire energy.

Figure 10 breaks down the energy consumed by the PU

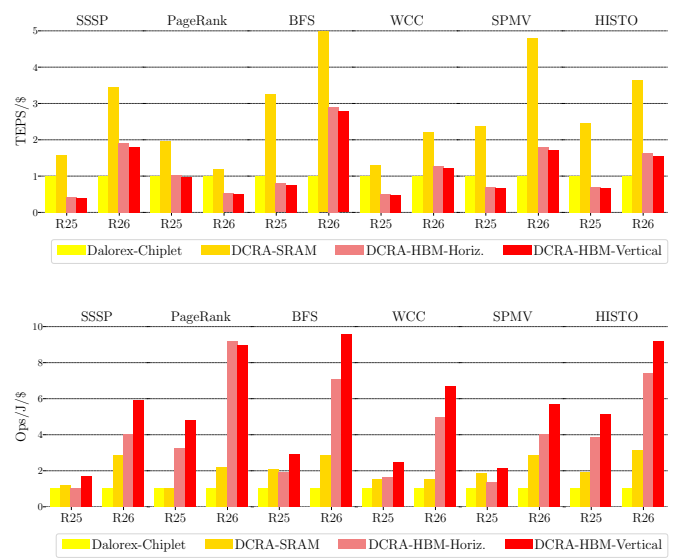


Fig. 9. Improvements in throughput/\$ and energy efficiency/\$, normalized to Dalorex. Dalorex and SRAM-only DCRA use a 64x64 configuration for RMAT-25 and 128x128 for RMAT-26. The HBM configurations use a 16x16 configuration for RMAT-25 and 32x32 for RMAT-26.

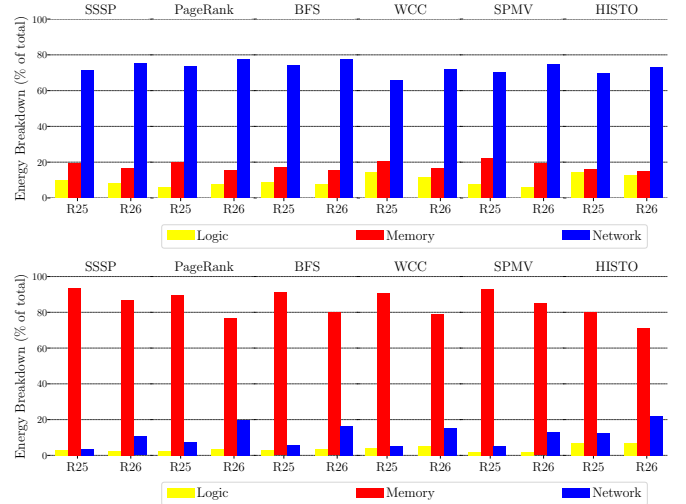


Fig. 10. Breakdown of the energy consumed by computing logic, memory, and network communication (including routing and wire energy). The plots break down the energy used by DCRA-SRAM (top) and DCRA-Horiz (bottom) with the same configurations of Figure 9. The Y-axis shows the percentage of the total energy spent on each component. The X-axis indicates the dataset.

logic, memory and network for both DCRA-SRAM and DCRA-HBM-Horiz. The SRAM-only integration scales out to use 16 \times more tiles than the version including HBM; thus, it spends much more energy on wires. Although not shown here, we observed that the HBM integration saturates the memory controller bandwidth. This makes the breakdown to be dominated by DRAM energy. PUs represent a small fraction on the energy consumption on both cases. Note that PUs are powered off by the TSU when idle, so they only consume energy while processing tasks.

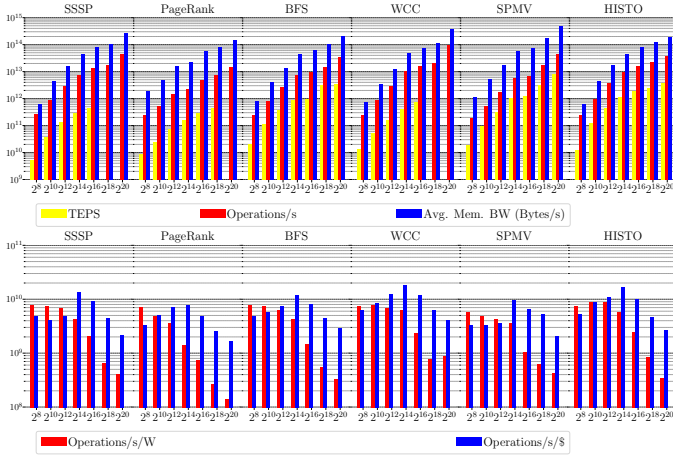


Fig. 11. Throughput in operations, traversed edges per second (TEPS), and the average on-chip memory bandwidth needed to achieve that. Note that the couple of datapoints without TEPS are partial run that the simulator could finish. Partial runs may show higher throughput as they have not reached the *cool-down* ending phase. The X-axis is the size of the DCRA grid used when analyzing strong scaling RMAT-26, ranging from 256 to over a million tiles. The Y-axis is logarithmic for both plots. The bottom plot shows throughput as a function of power and cost. Higher is better.

D. Strong Scaling Up to a Million Tiles

Throughput-per-watt likes small grids: From Figure 11 (bottom), we observe that when throughput-per-watt is the critical metric, staying within the smallest configuration that fits the dataset is the correct choice. The RMAT-26 dataset fits entirely on a 16x16 die with 8GB HBM. Throughput-per-watt drops significantly after using 2^{12} tiles, i.e., a chip package of 64x64 tiles. The inter-package links are more power-hungry than the links inside the package, hence, the drop in efficiency.

Throughput-per-dollar increases during superlinear performance scaling: Optimal throughput-per-dollar peaks at a 128x128 configuration (4 chip packages). This is because while the cost grows linearly with the number of chips, the performance grew super-linearly until that scaling step, where the decrease in footprint-per-tile also decreased the pressure in the memory controller of the HBM. At 128x128, RMAT-26 fits in SRAM. Beyond that, the gradually smaller footprint-per-tile reduces PU utilization since there are less parallel tasks to be executed. This leads to a less than linear scaling that makes the throughput-per-dollar to decrease.

Strong scaling for faster time-to-solution: For purposes of this experiment we take the extreme approach of parallelizing a dataset with 2^{26} vertices (and $\sim 2^{28}$ edges) across 2^{20} tiles. This shows that DCRA is suited for strong scaling, although it is not the most efficient way to use it.

Work Efficiency: The goal in graph applications is high TEPS, and not necessarily operations per second. TEPS is a measurement for how long it takes to process a certain dataset. The order in which vertices are processed matters for work efficiency, so throughput alone does not determine runtime. From Figure 11 (top), we can observe that for very large parallelizations of SSSP, BFS and WCC, the increase in throughput does not translate into an equal increase in

TEPS. (We can expect a similar trend for the datapoints that the simulator could not finish). Better work efficiency could be achieved by enforcing order with a barrier at the end of each epoch, but this would reduce the throughput. PageRank does have that barrier, and we observe a more steady increase in throughput and TEPS. For Histogram and SPMV, TEPS indicate total array elements divided by runtime, which correlates with throughput. This is because data updates are only relevant for the final result, what allows proxy updates not to get propagated to the owners until the last part of the execution (when proxy regions are invalidated). Histogram is a simpler kernel than SPMV, and so the reason for the trend is simply lack of work to be parallelized. SPMV achieves a remarkable scaling all the way to the million-tile configuration. The spike in throughput at the last datapoints is that we could dedicate more SRAM resources to task queues due to having a smaller data footprint-per-tile. We saw in Figure 7 that larger IQs had a big impact on SPMV performance.

Petabyte/s of memory bandwidth: We mentioned in the beginning of the paper that data-structure traversal have a high memory to compute ratio. We can observed in this plot how much memory bandwidth is required to maintain a high target throughput. Figure 11 (top) shows that for the 1-million-tile configuration, SPMV reads, on average, half a PB/s from their local memories. At peak, SPMV is reading 1.7 PB/s to perform 450 Teraops/s, of which 43 Teraops/s are dedicated to multiplication of non-zero matrix elements. It achieves that by drawing 37KW across 256 chip packages (power density stays in the tens of mW/mm², air cooling).

Comparing with the state-of-the-art: From the Graph500 list, the current best performance for BFS on **RMAT-26** is 884 GTEPS, which is achieved at the Tianhe Exa-node (Prototype@GraphV) [52]. The next entry features an undisclosed *High Throughput Computer* with four NVidia V100-SXM2, which delivers 392 GTEPS. For RMAT-26, our work performs 3161 GTEPS on a 512x512 grid (256 chips) and 3323 GTEPS on a 1024x1024 grid (256 chips). Given the assumed chip I/O and the number of chips, bringing the dataset on chip would take < 0.1 ms.

For smaller datasets like **RMAT-22**, although Graph500's best entry is at 1 GTEPS, we found other works showing up to 70 GTEPS [10] running the Enterprise [46] and Gunrock codes [86] on a 32GB NVIDIA Tesla V100-SXM3. For RMAT-22, the 64x64 configuration (single-chip) evaluated in Figure 6 would achieve 362 GTEPS. Note that this GPU runs at 1.6 GHz, while we assume 1 Ghz for our system.

VI. CONCLUSION

In this work we demonstrate that our data-centric architecture scales performance for sparse data applications even when processing datasets of 2^{26} vertices across 2^{20} PUs. This is $100\times$ larger than the prior largest parallelization of a problem of this size. We achieve this by leveraging the benefits of data-local execution while introducing a reconfigurable tile fabric that removes prior work's limitations. Our work introduces techniques for better work balance, scalable network

communication, and reconfigurable memory hierarchy. DCRA allows integrating extra DRAM on chip, drastically reducing the need to scale out when processing large datasets. Through our reconfigurable design, one can balance cost, performance and energy efficiency tradeoffs and tailor compile-time optimizations such as proxy, cache, and queue sizes.

REFERENCES

- [1] M. Abeydeera and D. Sanchez, "Chronos: Efficient speculative parallelism for accelerators," in *Proceedings of the Twenty-Fifth International Conference on Architectural Support for Programming Languages and Operating Systems*, 2020, pp. 1247–1262.
- [2] N. R. Adiga, G. Almási, G. S. Almási, Y. Aridor, R. Barik, D. Beece, R. Bellofatto, G. Bhanot, R. Bickford, M. Blumrich *et al.*, "An overview of the bluegene/l supercomputer," in *SC'02: Proceedings of the 2002 ACM/IEEE Conference on Supercomputing*. IEEE, 2002, pp. 60–60.
- [3] J. Ahn, S. Hong, S. Yoo, O. Mutlu, and K. Choi, "A scalable processing-in-memory accelerator for parallel graph processing," in *Proceedings of the 42nd Annual International Symposium on Computer Architecture*, 2015, pp. 105–117.
- [4] AMD, "Amd rome," 2018, <https://en.wikichip.org/wiki/amd/cores/rome>.
- [5] S. Ardalán, B. Vinnikota, T. Arabi, and E. Alon, "What is the right die-to-die interface? a comparison study," 2022, <https://www.opencompute.org/events/past-events/hipchips-chiplet-workshop-isca-conference>.
- [6] K. Asanovic, R. Bodik, B. C. Catanzaro, J. J. Gebis, P. Husbands, K. Keutzer, D. A. Patterson, W. L. Plishker, J. Shalf, S. W. Williams *et al.*, "The landscape of parallel computing research: A view from berkeley," *eScholarship, University of California*, 2006.
- [7] J. Balkind, K. Lim, F. Gao, J. Tu, D. Wentzlauff, M. Schaffner, F. Zaruba, and L. Benini, "OpenPiton+Ariane: The first open-source, SMP Linux-booting RISC-V system scaling from one to many cores," in *Third Workshop on Computer Architecture Research with RISC-V, CARRV*, vol. 19, 2019.
- [8] A. Benner, "Optical interconnect opportunities in supercomputers and high end computing," in *OFC/NFOEC*. IEEE, 2012, pp. 1–60.
- [9] B. Black, "Die stacking is happening," in *Intl. Symp. on Microarchitecture, Davis, CA*, 2013.
- [10] L. Burchard, J. Moe, D. T. Schroeder, K. Pogorelov, and J. Langguth, "ipug: Accelerating breadth-first graph traversals using manycore graph-core ipus," in *International Conference on High Performance Computing*. Springer, 2021, pp. 291–309.
- [11] L. P. Carloni, "The case for embedded scalable platforms," in *2016 53rd ACM/EDAC/IEEE Design Automation Conference (DAC)*. IEEE, 2016, pp. 1–6.
- [12] Cerebras Systems Inc., "The second generation wafer scale engine," <https://cerebras.net/wp-content/uploads/2021/04/Cerebras-CS-2-Whitepaper.pdf>.
- [13] R. Chaware, K. Nagarajan, and S. Ramalingam, "Assembly and reliability challenges in 3d integration of 28nm fpga die on a large high density 65nm passive interposer," in *2012 IEEE 62nd Electronic Components and Technology Conference*, 2012, pp. 279–283.
- [14] J. Choquette and W. Gandhi, "Nvidia A100 GPU: Performance & innovation for GPU computing," in *2020 IEEE Hot Chips 32 Symposium (HCS)*. IEEE Computer Society, 2020, pp. 1–43.
- [15] C. C. Chou, A. Jaleel, and M. K. Qureshi, "Cameo: A two-level memory organization with capacity of main memory and flexibility of hardware-managed cache," in *2014 47th Annual IEEE/ACM International Symposium on Microarchitecture*. IEEE, 2014, pp. 1–12.
- [16] E. G. Cota, P. Mantovani, and L. P. Carloni, "Exploiting private local memories to reduce the opportunity cost of accelerator integration," in *Proceedings of the 2016 International Conference on Supercomputing*, 2016, pp. 1–12.
- [17] V. Dadu, S. Liu, and T. Nowatzki, "Polygraph: Exposing the value of flexibility for graph processing accelerators," in *2021 ACM/IEEE 48th Annual International Symposium on Computer Architecture (ISCA)*. IEEE, 2021, pp. 595–608.
- [18] S. Davidson, S. Xie, C. Torng, K. Al-Hawai, A. Rovinski, T. Ajayi, L. Vega, C. Zhao, R. Zhao, S. Dai, A. Amarnath, B. Veluri, P. Gao, A. Rao, G. Liu, R. K. Gupta, Z. Zhang, R. Dreslinski, C. Batten, and M. B. Taylor, "The celerity open-source 511-core risc-v tiered accelerator fabric: Fast architectures and design methodologies for fast chips," *IEEE Micro*, vol. 38, no. 2, pp. 30–41, 2018.
- [19] Y. Demir, Y. Pan, S. Song, N. Hardavellas, J. Kim, and G. Memik, "Galaxy: A high-performance energy-efficient multi-chip architecture using photonic interconnects," in *Proceedings of the 28th ACM international conference on Supercomputing*, 2014, pp. 303–312.
- [20] M. Emani, V. Vishwanath, C. Adams, M. E. Papka, R. Stevens, L. Florescu, S. Jairath, W. Liu, T. Nama, and A. Sujeeth, "Accelerating scientific applications with sambanova reconfigurable dataflow architecture," *Computing in Science & Engineering*, vol. 23, no. 2, pp. 114–119, 2021.
- [21] Esperanto Technologies, "Esperanto's et-minion on-chip risc-v cores," <https://www.esperanto.ai/technology/>.
- [22] J. Frazelle, "Chip measuring contest: The benefits of purpose-built chips," *Queue*, vol. 19, no. 5, pp. 5–21, 2021.
- [23] S. Ghose, A. G. Yaglikçi, R. Gupta, D. Lee, K. Kudrolli, W. X. Liu, H. Hassan, K. K. Chang, N. Chatterjee, A. Agrawal *et al.*, "What your dram power models are not telling you: Lessons from a detailed experimental study," *Proceedings of the ACM on Measurement and Analysis of Computing Systems*, vol. 2, no. 3, pp. 1–41, 2018.
- [24] D. Giri, K.-L. Chiu, G. Di Guglielmo, P. Mantovani, and L. P. Carloni, "ESP4ML: Platform-based design of systems-on-chip for embedded machine learning," in *DATE*. IEEE Press, 2020.
- [25] W. Gomes, A. Koker, P. Stover, D. Ingerly, S. Siers, S. Venkataraman, C. Peltó, T. Shah, A. Rao, F. O'Mahony *et al.*, "Ponte vecchio: A multi-tile 3d stacked processor for exascale computing," in *2022 IEEE International Solid-State Circuits Conference (ISSCC)*, vol. 65. IEEE, 2022, pp. 42–44.
- [26] L. Gwennap, "Groq rocks neural networks," *Microprocessor Report, Tech. Rep.*, jan, 2020.
- [27] T. J. Ham, L. Wu, N. Sundaram, N. Satish, and M. Martonosi, "Graphiconado: A high-performance and energy-efficient accelerator for graph analytics," in *Proceedings of the 49th Annual International Symposium on Microarchitecture*, ser. MICRO, 2016. [Online]. Available: <https://doi.org/10.1109/MICRO.2016.7783759>
- [28] "High-Bandwidth Memory (HBM)," 2015, <https://www.amd.com/Documents/High-Bandwidth-Memory-HBM.pdf>.
- [29] X. Hu, D. Stow, and Y. Xie, "Die stacking is happening," *IEEE micro*, vol. 38, no. 1, pp. 22–28, 2018.
- [30] Intel, "Intel kaby lake g," 2018, https://en.wikichip.org/wiki/intel/cores/kaby_lake_g.
- [31] Isine, "Die yield calculator," <https://isine.com/resources/die-yield-calculator/>.
- [32] JEDEC, "Standard high bandwidth memory specification jesd235a," 2015.
- [33] S. W. Jones, "Lithovision: Economics in the 3d era," <https://semiwiki.com/wp-content/uploads/2020/03/Lithovision-2020.pdf>.
- [34] N. P. Jouppi, C. Young, N. Patil, D. Patterson, G. Agrawal, R. Bajwa, S. Bates, S. Bhatia, N. Boden, A. Borchers *et al.*, "In-datacenter performance analysis of a tensor processing unit," in *Proceedings of the 44th annual international symposium on computer architecture*, 2017, pp. 1–12.
- [35] D.-H. Kim, B. Song, H.-a. Ahn, W. Ko, S. Do, S. Cho, K. Kim, S.-H. Oh, H.-Y. Joo, G. Park, J.-H. Jang, Y.-H. Kim, D. Lee, J. Jung, Y. Kwon, Y. Kim, J. Jung, S. O. S. Lee, J. Lim, J. Son, J. Min, H. Do, J. Yoon, I. Hwang, J. Park, H. Shim, S. Yoon, D. Choi, J. Lee, S. Woo, E. Hong, J. Choi, J.-S. Kim, S. Han, J. Bang, B. Park, J. Kim, S.-K. Choi, G.-H. Han, Y.-C. Sung, W.-I. Bae, J.-D. Lim, S. Lee, C. Yoo, S. J. Hwang, and J. Lee, "A 16gb 9.5gb/s/pin lpddr5x sdram with low-power schemes exploiting dynamic voltage-frequency scaling and offset-calibrated readout sense amplifiers in a fourth generation 10nm dram process," in *2022 IEEE International Solid-State Circuits Conference (ISSCC)*, vol. 65, 2022, pp. 448–450.
- [36] S. Kim, S. Kim, K. Cho, T. Shin, H. Park, D. Lho, S. Park, K. Son, G. Park, and J. Kim, "Processing-in-memory in high bandwidth memory (pim-hbm) architecture with energy-efficient and low latency channels for high bandwidth system," in *2019 IEEE 28th Conference on Electrical Performance of Electronic Packaging and Systems (EPEPS)*, 2019, pp. 1–3.
- [37] S. Knowles, "Graphcore," in *2021 IEEE Hot Chips 33 Symposium (HCS)*. IEEE, 2021, pp. 1–25.
- [38] S. Kumar, H. Zhao, A. Shriraman, E. Matthews, S. Dwarkadas, and L. Shannon, "Amoeba-cache: Adaptive blocks for eliminating waste in the memory hierarchy," in *2012 45th Annual IEEE/ACM International Symposium on Microarchitecture*. IEEE, 2012, pp. 376–388.
- [39] J. H. Lau, "Status and outlooks of flip chip technology," *IPC EXPO Proceedings, February 2017*, pp. 1–20, 2017.

- [40] P. Lawrence, B. Sergey, R. Motwani, and T. Winograd, "The pagerank citation ranking: Bringing order to the web," Stanford University, Technical Report, 1998.
- [41] C.-C. Lee, C. Hung, C. Cheung, P.-F. Yang, C.-L. Kao, D.-L. Chen, M.-K. Shih, C.-L. C. Chien, Y.-H. Hsiao, L.-C. Chen, M. Su, M. Alfano, J. Siegel, J. Din, and B. Black, "An overview of the development of a gpu with integrated hbm on silicon interposer," in *2016 IEEE 66th Electronic Components and Technology Conference (ECTC)*, 2016, pp. 1439–1444.
- [42] D. U. Lee, H. S. Cho, J. Kim, Y. J. Ku, S. Oh, C. D. Kim, H. W. Kim, W. Y. Lee, T. K. Kim, T. S. Yun *et al.*, "22.3 a 128gb 8-high 512gb/s hbm2e dram with a pseudo quarter bank structure, power dispersion and an instruction-based at-speed pmbist," in *2020 IEEE International Solid-State Circuits Conference (ISSCC)*. IEEE, 2020, pp. 334–336.
- [43] J. Leskovec, D. Chakrabarti, J. Kleinberg, C. Faloutsos, and Z. Ghahramani, "Kronecker graphs: An approach to modeling networks," *Journal of Machine Learning Research (JMLR)*, vol. 11, pp. 985–1042, Mar. 2010.
- [44] C. Lichtenau, A. Buyuktosunoglu, R. Bertran, P. Figuli, C. Jacobi, N. Papandreou, H. Pozidis, A. Saporito, A. Sica, and E. Tzortzatos, "Ai accelerator on ibm telum processor: industrial product," in *Proceedings of the 49th Annual International Symposium on Computer Architecture*, 2022, pp. 1012–1028.
- [45] S. Lie, "Multi-million core, multi-wafer ai cluster," in *2021 IEEE Hot Chips 33 Symposium (HCS)*. IEEE Computer Society, 2021, pp. 1–41.
- [46] H. Liu and H. H. Huang, "Enterprise: breadth-first graph traversal on gpus," in *Proceedings of the International Conference for High Performance Computing, Networking, Storage and Analysis*, 2015, pp. 1–12.
- [47] R. Mahajan, R. Sankman, N. Patel, D.-W. Kim, K. Aygun, Z. Qian, Y. Mekonnen, I. Salama, S. Sharan, D. Iyengar *et al.*, "Embedded multi-die interconnect bridge (emib)—a high density, high bandwidth packaging interconnect," in *2016 IEEE 66th Electronic Components and Technology Conference (ECTC)*. IEEE, 2016, pp. 557–565.
- [48] A. Manocha, T. Sorensen, E. Tureci, O. Matthews, J. L. Aragón, and M. Martonosi, "Graphattack: Optimizing data supply for graph applications on in-order multicore architectures," *ACM Transactions on Architecture and Code Optimization (TACO)*, vol. 18, no. 4, pp. 1–26, 2021.
- [49] M. McKeown, A. Lavrov, M. Shahrad, P. J. Jackson, Y. Fu, J. Balkind, T. M. Nguyen, K. Lim, Y. Zhou, and D. Wentzlauff, "Power and energy characterization of an open source 25-core manycore processor," in *HPCA*, 2018, pp. 762–775.
- [50] R. Meade, S. Ardlan, M. Davenport, J. Fini, C. Sun, M. Wade, A. Wright-Gladstein, and C. Zhang, "Teraphy: a high-density electronic-photonics chiplet for optical i/o from a multi-chip module," in *2019 Optical Fiber Communications Conference and Exhibition (OFC)*. IEEE, 2019, pp. 1–3.
- [51] Micron, "High Bandwidth Memory with ECC," 2018, https://media-www.micron.com/-/media/client/global/documents/products/data-sheet/dram/hbm2e/8gb_and_16gb_hbm2e_dram.pdf.
- [52] R. C. Murphy, K. B. Wheeler, B. W. Barrett, and J. A. Ang, "Introducing the Graph 500," <http://www.graph500.org/specifications>, Cray User's Group (CUG), 2010.
- [53] S. Naffziger, N. Beck, T. Burd, K. Lepak, G. H. Loh, M. Subramony, and S. White, "Pioneering chiplet technology and design for the amd epyc™ and ryzen™ processor families," in *Proceedings of the 48th Annual International Symposium on Computer Architecture*, ser. ISCA '21. IEEE Press, 2021, p. 57–70.
- [54] N. Nassif, A. O. Munch, C. L. Molnar, G. Pasdast, S. V. Lyer, Z. Yang, O. Mendoza, M. Huddart, S. Venkataraman, S. Kandula *et al.*, "Sapphire rapids: The next-generation intel xeon scalable processor," in *2022 IEEE International Solid-State Circuits Conference (ISSCC)*, vol. 65. IEEE, 2022, pp. 44–46.
- [55] Q. M. Nguyen and D. Sanchez, "Pipette: Improving core utilization on irregular applications through intra-core pipeline parallelism," in *2020 53rd Annual IEEE/ACM International Symposium on Microarchitecture (MICRO)*. IEEE, 2020, pp. 596–608.
- [56] Q. M. Nguyen and D. Sanchez, "Fifer: Practical acceleration of irregular applications on reconfigurable architectures," in *MICRO-54: 54th Annual IEEE/ACM International Symposium on Microarchitecture*, ser. MICRO '21. New York, NY, USA: Association for Computing Machinery, 2021, p. 1064–1077. [Online]. Available: <https://doi.org/10.1145/3466752.3480048>
- [57] C.-S. Oh, K. C. Chun, Y.-Y. Byun, Y.-K. Kim, S.-Y. Kim, Y. Ryu, J. Park, S. Kim, S. Cha, D. Shin *et al.*, "22.1 a 1.1 v 16gb 640gb/s hbm2e dram with a data-bus window-extension technique and a synergetic on-die ecc scheme," in *2020 IEEE International Solid-State Circuits Conference (ISSCC)*. IEEE, 2020, pp. 330–332.
- [58] Open Compute Group, "Bunch of wires phy specification," https://opencompute.github.io/ODSA-BoW/bow_specification.html.
- [59] M. Orenes-Vera, A. Manocha, J. Balkind, F. Gao, J. L. Aragón, D. Wentzlauff, and M. Martonosi, "Tiny but mighty: designing and realizing scalable latency tolerance for manycore socs," in *ISCA*, 2022, pp. 817–830.
- [60] M. Orenes-Vera, E. Tureci, D. Wentzlauff, and M. Martonosi, "Dalorex: A data-local program execution and architecture for memory-bound applications," *arXiv:2207.13219. To appear at the 29th IEEE International Symposium on High-Performance Computer Architecture (HPCA)*, 2022.
- [61] Y. Ou, S. Agwa, and C. Batten, "Implementing low-diameter on-chip networks for manycore processors using a tiled physical design methodology," in *2020 14th IEEE/ACM International Symposium on Networks-on-Chip (NOCS)*. IEEE, 2020, pp. 1–8.
- [62] M. M. Ozdal, S. Yesil, T. Kim, A. Ayupov, J. Greth, S. Burns, and O. Ozturk, "Energy efficient architecture for graph analytics accelerators," *ACM SIGARCH Computer Architecture News*, vol. 44, no. 3, pp. 166–177, 2016.
- [63] M. O'Connor, N. Chatterjee, D. Lee, J. Wilson, A. Agrawal, S. W. Keckler, and W. J. Dally, "Fine-grained dram: Energy-efficient dram for extreme bandwidth systems," in *2017 50th Annual IEEE/ACM International Symposium on Microarchitecture (MICRO)*. IEEE, 2017, pp. 41–54.
- [64] S. Pal, D. Petrisko, M. Tomei, P. Gupta, S. S. Iyer, and R. Kumar, "Architecting waferscale processors—a gpu case study," in *2019 IEEE International Symposium on High Performance Computer Architecture (HPCA)*. IEEE, 2019, pp. 250–263.
- [65] M.-J. Park, H. S. Cho, T.-S. Yun, S. Byeon, Y. J. Koo, S. Yoon, D. U. Lee, S. Choi, J. Park, J. Lee *et al.*, "A 192-gb 12-high 896-gb/s hbm3 dram with a tsv auto-calibration scheme and machine-learning-based layout optimization," in *2022 IEEE International Solid-State Circuits Conference (ISSCC)*, vol. 65. IEEE, 2022, pp. 444–446.
- [66] A. Patrizio, "High-bandwidth memory (hbm) delivers impressive performance gains," <https://semiengineering.com/whats-next-for-high-bandwidth-memory/>.
- [67] J. T. Pawlowski, "Hybrid memory cube (hmc)," in *2011 IEEE Hot Chips 23 Symposium (HCS)*. IEEE, 2011, pp. 1–24.
- [68] C. Premachandran, T. Tran-Quinn, L. Burrell, and P. Justison, "A comprehensive wafer level reliability study on 65nm silicon interposer," in *2019 IEEE International Reliability Physics Symposium (IRPS)*, 2019, pp. 1–8.
- [69] V. Puente, R. Beivide, J. A. Gregorio, J. Prellezo, J. Duato, and C. Izu, "Adaptive bubble router: a design to improve performance in torus networks," in *Proceedings of the 1999 International Conference on Parallel Processing*. IEEE, 1999, pp. 58–67.
- [70] S. Rahman, N. Abu-Ghazaleh, and R. Gupta, "Graphpulse: An event-driven hardware accelerator for asynchronous graph processing," in *2020 53rd Annual IEEE/ACM International Symposium on Microarchitecture (MICRO)*. IEEE, 2020, pp. 908–921.
- [71] A. Shah, "Chipmakers Looking at New Architecture to Drive Computing Ahead," 2022, <https://www.hpcwire.com/2022/11/23/chipmakers-looking-at-new-architecture-to-drive-computing-ahead/>.
- [72] D. D. Sharma, "Pci express 6.0 specification: A low-latency, high-bandwidth, high-reliability, and cost-effective interconnect with 64.0 gt/s pam-4 signaling," *IEEE Micro*, vol. 41, no. 1, pp. 23–29, 2020.
- [73] D. D. Sharma, G. Pasdast, Z. Qian, and K. Aygun, "Universal chiplet interconnect express (ucie): An open industry standard for innovations with chiplets at package level," *IEEE Transactions on Components, Packaging and Manufacturing Technology*, vol. 12, no. 9, pp. 1423–1431, 2022.
- [74] K. Shiba, T. Omori, K. Ueyoshi, S. Takamaeda-Yamazaki, M. Motomura, M. Hamada, and T. Kuroda, "A 96-mb 3d-stacked sram using inductive coupling with 0.4-v transmitter, termination scheme and 12:1 serdes in 40-nm cmos," *IEEE Transactions on Circuits and Systems I: Regular Papers*, vol. 68, no. 2, pp. 692–703, 2020.
- [75] G. M. Slota, S. Rajamanickam, and K. Madduri, "BFS and coloring-based parallel algorithms for strongly connected components and related problems," in *2014 IEEE 28th International Parallel and Distributed Processing Symposium, Phoenix, AZ, USA, May 19-23,*

2014. IEEE Computer Society, 2014, pp. 550–559. [Online]. Available: <https://doi.org/10.1109/IPDPS.2014.64>
- [76] K. Sohn, W.-J. Yun, R. Oh, C.-S. Oh, S.-Y. Seo, M.-S. Park, D.-H. Shin, W.-C. Jung, S.-H. Shin, J.-M. Ryu, H.-S. Yu, J.-H. Jung, H. Lee, S.-Y. Kang, Y.-S. Sohn, J.-H. Choi, Y.-C. Bae, S.-J. Jang, and G. Jin, “A 1.2 v 20 nm 307 gb/s hbm dram with at-speed wafer-level io test scheme and adaptive refresh considering temperature distribution,” *IEEE Journal of Solid-State Circuits*, vol. 52, no. 1, pp. 250–260, 2017.
- [77] A. Stillmaker and B. Baas, “Scaling equations for the accurate prediction of cmos device performance from 180 nm to 7 nm,” *Integration*, vol. 58, pp. 74–81, 2017.
- [78] D. Stow, Y. Xie, T. Siddiqua, and G. H. Loh, “Cost-effective design of scalable high-performance systems using active and passive interposers,” in *2017 IEEE/ACM International Conference on Computer-Aided Design (ICCAD)*, 2017, pp. 728–735.
- [79] J. A. Stratton, C. Rodrigues, I.-J. Sung, N. Obeid, L.-W. Chang, N. Anssari, G. D. Liu, and W.-m. Hwu, “Parboil: A revised benchmark suite for scientific and commercial throughput computing,” University of Illinois at Urbana-Champaign, Tech. Rep. IMPACT-12-01, 2012.
- [80] R. Swaminathan and J. Wu, “Chiplet’s march to amd 3d v-cache and beyond,” 2022, <https://www.opencompute.org/events/past-events/hipchips-chiplet-workshop-isca-conference>.
- [81] N. Talati, K. May, A. Behroozi, Y. Yang, K. Kaszyk, C. Vasiladiotis, T. Verma, L. Li, B. Nguyen, J. Sun, J. M. Morton, A. Ahmadi, T. Austin, M. O’Boyle, S. Mahlke, T. Mudge, and R. Dreslinski, “Prodigy: Improving the memory latency of data-indirect irregular workloads using hardware-software co-design,” in *2021 IEEE International Symposium on High-Performance Computer Architecture (HPCA)*. IEEE, 2021, pp. 654–667.
- [82] E. Talpes, D. Williams, and D. D. Sarma, “Dojo: The microarchitecture of tesla exa-scale computer,” in *2022 IEEE Hot Chips 34 Symposium (HCS)*. IEEE Computer Society, 2022, pp. 1–28.
- [83] T. Tang and Y. Xie, “Cost-aware exploration for chiplet-based architecture with advanced packaging technologies,” *arXiv preprint arXiv:2206.07308*, 2022.
- [84] Y. Tian, A. Balmin, S. A. Corsten, S. Tatikonda, and J. McPherson, “From” think like a vertex” to” think like a graph”,” *Proceedings of the VLDB Endowment*, vol. 7, no. 3, pp. 193–204, 2013.
- [85] P. Vivet, E. Guthmuller, Y. Thonnart, G. Pillonnet, C. Fuguet, I. Miro-Panades, G. Moritz, J. Durupt, C. Bernard, D. Varreau, J. Pontes, S. Thuries, D. Coriat, M. Harrand, D. Dutoit, D. Lattard, L. Arnaud, J. Charbonnier, P. Coudrain, A. Garnier, F. Berger, A. Gueugnot, A. Greiner, Q. L. Meunier, A. Farcy, A. Arriordaz, S. Chéramy, and F. Clermidy, “Intact: A 96-core processor with six chiplets 3d-stacked on an active interposer with distributed interconnects and integrated power management,” *IEEE Journal of Solid-State Circuits*, vol. 56, no. 1, pp. 79–97, 2021.
- [86] Y. Wang, A. Davidson, Y. Pan, Y. Wu, A. Riffel, and J. D. Owens, “Gunrock: A high-performance graph processing library on the gpu,” in *Proceedings of the 21st ACM SIGPLAN symposium on principles and practice of parallel programming*, 2016, pp. 1–12.
- [87] J. Wilson, “High-bandwidth density, energy-efficient, short-reach signaling that enables massively scalable parallelism,” 2022, <https://www.opencompute.org/events/past-events/hipchips-chiplet-workshop-isca-conference>.
- [88] Q. Xie, X. Lin, Y. Wang, S. Chen, M. J. Dousti, and M. Pedram, “Performance comparisons between 7-nm finfet and conventional bulk cmos standard cell libraries,” *IEEE Transactions on Circuits and Systems II: Express Briefs*, vol. 62, no. 8, pp. 761–765, 2015.
- [89] Y. Yokoyama, M. Tanaka, K. Tanaka, M. Morimoto, M. Yabuuchi, Y. Ishii, and S. Tanaka, “A 29.2 mb/mm2 ultra high density sram macro using 7nm finfet technology with dual-edge driven wordline/bitline and write/read-assist circuit,” in *2020 IEEE Symposium on VLSI Circuits*, 2020, pp. 1–2.
- [90] F. Zaruba and L. Benini, “The cost of application-class processing: Energy and performance analysis of a linux-ready 1.7-ghz 64-bit risc-v core in 22-nm fdsoi technology,” *IEEE Transactions on Very Large Scale Integration (VLSI) Systems*, vol. 27, no. 11, pp. 2629–2640, Nov 2019, <https://github.com/openhwgroup/cva6>.
- [91] F. Zaruba and L. Benini, “Ariane: An open-source 64-bit RISC-V application class processor and latest improvements,” 2018, technical talk at the RISC-V Workshop <https://www.youtube.com/watch?v=8HpvRNh0ux4>.
- [92] F. Zaruba, F. Schuiki, and L. Benini, “Manticore: A 4096-core risc-v chiplet architecture for ultraefficient floating-point computing,” *IEEE Micro*, vol. 41, no. 2, pp. 36–42, 2020.
- [93] F. Zaruba, F. Schuiki, T. Hoefler, and L. Benini, “Snitch: A tiny pseudo dual-issue processor for area and energy efficient execution of floating-point intensive workloads,” *IEEE Transactions on Computers*, 2020.
- [94] M. Zhang, Y. Zhuo, C. Wang, M. Gao, Y. Wu, K. Chen, C. Kozyrakis, and X. Qian, “Graphp: Reducing communication for pim-based graph processing with efficient data partition,” in *2018 IEEE International Symposium on High Performance Computer Architecture (HPCA)*. IEEE, 2018, pp. 544–557.
- [95] Y. Zhu, B. Wang, D. Li, and J. Zhao, “Integrated thermal analysis for processing in die-stacking memory,” in *Proceedings of the Second International Symposium on Memory Systems*, 2016, pp. 402–414.
- [96] Y. Zhuo, C. Wang, M. Zhang, R. Wang, D. Niu, Y. Wang, and X. Qian, “Graphq: Scalable pim-based graph processing,” in *Proceedings of the 52nd Annual IEEE/ACM International Symposium on Microarchitecture*, 2019, pp. 712–725.